Sources of nitrous acid (HONO) in the upper boundary layer and lower free troposphere of the North China Plain: insights from the Mount Tai Observatory

Ying Jiang[1], Likun Xue[1,4*], Rongrong Gu[1], Mengwei Jia[2], Yingnan Zhang[1], Liang Wen[1], Penggang Zheng[1], Tianshu Chen[1], Hongyong Li[1], Ye Shan[1], Yong Zhao[3], Zhaoxin Guo[3], Yujian Bi[3], Hengde Liu[3], Aijun Ding[2,4], Qingzhu Zhang[1], Wenxing Wang[1]

[1]Environment Research Institute, Shandong University, Qingdao, Shandong, 266237, China

[2]School of Atmospheric Sciences, Nanjing University, Nanjing, 210023, China

[3]Taishan National Reference Climatological Station, Tai'an, Shandong, 271000, China

[4]Collaborative innovation Center for climate Change, Jiangsu Province, Nanjing, 210023, China

*Correspondence to: Likun Xue (xuelikun@sdu.edu.cn)

Abstract: Nitrous acid (HONO) is a significant precursor of atmospheric "detergent" OH radicals, and plays a vital role in tropospheric chemistry. The current knowledge about the daytime HONO sources is incomplete, and its impact on the tropospheric radical chemistry has not been fully quantified. Existing observational studies of HONO were mostly conducted at the surface, with few efforts focusing on the high-elevation atmospheres. In order to better understand the characteristics and sources of HONO in the upper boundary layer and lower free troposphere, two intensive field observations were carried out at the summit of Mt. Tai (1534 m a.s.l.), the peak of the North China Plain, in winter 2017 and spring 2018. HONO showed moderate concentration levels (average ± standard deviation: 0.15±0.15 and 0.13±0.15 ppbv), with maximum values of 1.14 and 3.23 ppbv in winter and spring, respectively. Diurnal variation patterns with broad noontime maxima and lower nighttime concentrations were observed during both campaigns, which is distinct from most of the previous studies at the ground level. The WRF-FLEXPART simulations indicated the combined effects of the planetary boundary layer evolution and valley breeze on the daytime HONO peak. A photostationary state (PSS) analysis suggested the strong unknown daytime HONO source with production rates of 0.45±0.25 ppb/h in winter and 0.64±0.49 ppb/h in spring. Correlation analysis supported the important role of photo-enhanced heterogeneous conversion of NO_2 to HONO on the aerosol surface at this high-elevation site. HONO photolysis is the predominant primary source of OH radical and plays a major role in the radical chemistry at Mt. Tai. The model only considering homogenous HONO source predicted much lower levels of the HO_x

radicals and atmospheric oxidation capacity, compared to the model constrained with measured HONO data. This study sheds light on the characteristics, sources, chemistry, and impacts of HONO in the upper boundary layer and lower free troposphere in the NCP region.

1   Introduction

Nitrous acid (HONO) is an important reactive trace gas in the Earth's atmosphere and plays a pivotal role in the tropospheric oxidation chemistry. Photolysis of HONO by sunlight releases the hydroxyl radical (OH), which initiates the oxidation reaction cycles, resulting in the degradation of various primary contaminants and formation of secondary pollutants such as ozone (O_3) and secondary aerosols (Alicke et al., 2003). HONO can react with amines to form nitrosamines, which are mutagenic and carcinogenic, and thus affects human health (Sleiman et al., 2010). HONO is also a key player in the biosphere-atmosphere interactions and the biogeochemical cycle via dry and wet depositions as well as soil microbial processes (Sörgel et al., 2015). Therefore, it is of high significance to better understand the characteristics, sources, sinks, and environmental consequences of tropospheric HONO.

In comparison to the sink processes that have been relatively well understood, the sources of ambient HONO are still under extensive exploration and discussions. In the ambient atmosphere, HONO can be either directly emitted from various processes such as combustion and soil emissions (Su et al., 2011; Nie et al., 2015), or formed from the photolysis and chemical reactions of reactive nitrogen-containing substances. The gas-phase reaction of NO with OH (R1) has long been known as a significant formation pathway of HONO (Platt et al., 1980), which forms a pseudo-steady state with the fast photolysis of HONO under sunlight (R2) and the reactions with OH (R3) during the daytime. The HONO concentrations in photostationary state (PSS; [HONO]$_{PSS}$) can be calculated by Eq. (E1). However, the field observations in the last decade have indicated that the [HONO]$_{PSS}$ can only account for a small portion of the measured concentrations in a variety of environments (Kleffmann et al., 2005; Zhou et al., 2007; Michoud et al., 2014), suggesting the action of additional daytime HONO sources. To explain the observed HONO levels, some new formation mechanisms have been proposed and tested in lab or through field studies (Bejan et al., 2006; Monge et al., 2010; Su et al., 2011; Li et al., 2014). Among them, a widely well-received HONO source is the heterogeneous reactions of NO_2 on various wet surfaces (R4), including ground, buildings, urban grime, and aerosol surfaces (Villena et al., 2011; Wong et al., 2012; Liu et al., 2014; Baergen and Donaldson, 2016). However, the contributions of the individual surface types to the ambient HONO formation have not been figured out. Most previous studies suggested the dominance of ground surface in the heterogeneous HONO formation at the ground level (Alicke et al., 2003; Elshorbany et al., 2009; Ziemba et al., 2010), while some studies argued that aerosol surface may

also play an important role (Colussi et al., 2013; Liu et al., 2014; Tong et al., 2016; Lu et al., 2018).

$$NO + OH \xrightarrow{M} HONO \qquad (R1)$$

$$HONO \xrightarrow{hv} NO + OH \qquad (R2)$$

$$HONO + OH \rightarrow NO_2 + H_2O \qquad (R3)$$

$$[HONO]_{PSS} = \frac{[NO] \times [OH] \times K_{NO+OH}}{J_{HONO} + [OH] \times K_{OH+HONO}} \qquad (E1)$$

$$2NO_2(g) + H_2O \text{ (surface)} \rightarrow HONO(g) + HNO_3 \text{ (surface)} \qquad (R4)$$
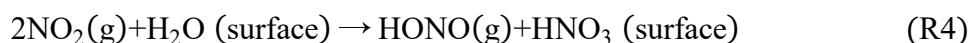
Currently, the field observational studies of HONO were mainly conducted at the surface level, with few efforts made in the high elevations such as upper planetary boundary layer (PBL) and lower free troposphere (FT). This hindered a thorough understanding of the characteristics, processes, and environmental impacts of tropospheric HONO. First, it can be easily expected that the HONO concentrations should be rather low in the upper PBL and lower FT, given the short lifetime of HONO under sunlight. This has been confirmed by the limited measurement studies at mountaintop and aboard aircraft (Acker et al., 2006; Zhou et al., 2007; Ye et al., 2016; Ye et al., 2018). Field observations at high-elevation sites could provide direct constraints for better understanding the vertical distribution and transport processes of HONO. Second, upper PBL and lower FT are free from the terrestrial (especially ground) surfaces and hence provide an ideal opportunity to evaluate the role of aerosol particles in the heterogeneous formation of HONO. Third, the impacts of HONO on the atmospheric oxidation capacity (AOC) in the upper PBL and lower FT have not been fully quantified. Existing modelling studies may underestimate the AOC of high-altitude atmospheres owing to the lack of observational data constraints (Kukui et al., 2014). Consequently, in-situ observations of HONO in the upper PBL and lower FT are very important to achieve a comprehensive understanding of the tropospheric oxidation chemistry.

To investigate the chemical and physical processes in the upper PBL and lower FT over the North China Plain (NCP), one of the most urbanized and polluted regions in China, two intensive field campaigns were carried out at Mt. Tai, the highest mountain over the region, in winter 2017 and spring 2018. This is a part of the Integrated Measurement Campaigns of Air Pollution Complex over the coastal regions of East China (iMAPEC), that aimed to deploy multiple advanced measurement platforms to investigate the three-dimensional distributions and processes governing the formation of regional air pollution over eastern China. A large suite of chemical species and physical properties were measured during the campaigns. This paper describes the measurement results of HONO and related parameters, which are the first report of HONO

chemistry in the upper PBL and lower FT in the NCP region. Several models including WRF-FLEXPART, PSS calculation, and Master Chemical Mechanism (MCM) box model were used to illustrate the origins, formation, and impacts of HONO. Overall, this study demonstrates the moderate pollution levels of HONO in the upper PBL and lower FT in the NCP, and provides some new insights into the roles of aerosol surface in the HONO formation as well as the significant effects of HONO photolysis on the atmospheric oxidation capacity in the high-altitude atmospheres.

2 Methodology

2.1 Site description

The Mt. Tai Observatory has been widely used as a sampling location to investigate the regional air pollution in the North China Plain region in the past decade (e.g., Gao et al., 2005; Sun et al., 2016; Wen et al., 2018). It is built at the summit of Mount Tai (36°16′ N, 117°6′ E, 1534 m a.s.l.), which is at the center of the NCP (see Fig. 1). The geographical location and altitude of Mount Tai make it representative of the regional background air of the region, and it is well within the upper planetary boundary layer during daytime on sunny days and in the residual layer or free troposphere at night. There are some local emissions from small restaurants and temples at the mountain, but the station is situated in the less frequently visited eastern part of the summit and thus the impact of local anthropogenic emissions can be neglected (Gao et al., 2005). The city of Tai'an (population: over 5.5 million) is located at the foot of Mt. Tai, about 15 km to the south, and the capital city of Shandong province, Ji'nan (population: over 7.4 million), is situated ~60 km to the north. It should be noted that a 1-yr continuous HONO measurement campaign had been conducted from September 2015 to August 2016 at an urban site of Ji'nan using the the same instrument (Li et al., 2018a), and their results are compared here with those at Mt. Tai to infer the vertical distributions of HONO in the NCP region. Details of the Mt. Tai Observatory can be found in Gao et al. (2005), Zhou et al. (2010), and Sun et al. (2016). Two intensive field measurement campaigns were conducted during 1st-31st December in 2017 and from 5th March to 8th April in 2018.

2.2 Measurement techniques

A large suite of chemical, physical, and meteorological parameters were measured in real-time during the campaigns. Here we briefly describe the measurement techniques for the species that were used in the present study. HONO was measured by a long path absorption photometer (LOPAP-03, *QUMA GmbH, Germany*). It detects HONO based on the wet chemistry theory, and two channels are designed to eliminate the possible interferences. The detailed description of the LOPAP instrument has been provided by Heland et al. (2001), and it has been successfully applied in various environments (Kleffmann et al., 2005; Li et al.,

2018a; Wen et al., 2019; Liu et al., 2019). During the present study, manual calibrations were performed using 1000 mg/L nitrite standard solutions every four days to examine the sensitivity of the detector, and the small drift of the baseline was corrected by regular automatic flushing with ultrapure nitrogen (purity of 99.999%), which was done for 30 min at a time interval of 11 h 30 min. The detection limit is 3 ppt at a time resolution of 30 s, and the measurement precision and accuracy are 1% and 10%, respectively.

Nitric oxide (NO) and total nitrogen oxides (NO_y) were measured by a commercial instrument (*Model T200U, Advanced Pollution Instrumentation (API), USA*), equipped with an externally placed molybdenum oxide catalytic converter. Nitrogen dioxide (NO_2) was monitored by a cavity-attenuated phase-shift spectroscopy that is highly selective for true NO_2 (*Model T500U, API, USA*). O_3 was measured by an UV photometric analyzer (*Model T400, API, USA*). CO was measured by a gas filter correlation, non-dispersive infrared analyzer (*Model 300EU, API, USA*). SO_2 was measured by an ultraviolet fluorescence analyzer (*Model 43C, Thermo Electron Corporation, USA*). The fine particle ($PM_{2.5}$) mass concentration was measured using a Synchronized Hybrid Ambient Real-time Particulate monitor (SHARP; *Thermo Scientific Model 5030*). Inorganic water-soluble ions (i.e., NO_3^-, SO_4^{2+}, NH_4^+, etc.) in $PM_{2.5}$ together with acid and alkaline gases (i.e., HNO_3, NH_3, etc.) were detected by a Monitor for AeRosols and GAses (*MARGA, ADI20801, Applikon-ECN, Netherlands*). The particle number size distributions (5-10000 nm) were measured by a Wide-Range Particle Spectrometer (*WPS, Model 1000XP, MSP Corporation, USA*), which were used to calculate the aerosol surface area density with an assumption that the particles are of spherical shape. Methane and C_2-C_{10} non-methane hydrocarbons (NMHCs) were measured by taking ambient air samples in stainless steel canisters on selected days, followed by chemical analysis by GC-FID/ECD/MS in the laboratory of University of California at Irvine (Simpson et al., 2010). C_1-C_8 carbonyl compounds were observed offline by absorbing ambient air into *2,4-DNPH* sorbent cartridge followed by HPLC analysis (Yang et al., 2018). Meteorological data including temperature, relative humidity (RH), pressure, and wind speed and direction were provided by Taishan National Reference Climatological Station. Photolysis frequency of NO_2 ($J(NO_2)$) was monitored with a filter radiometer (*Meteorologie Consult GmbH, Germany*), and the measurements were only available during the spring campaign. All of these techniques have been successfully used in many previous studies, where details of the operation, quality assurance and quality control procedures can be found (e.g., Li et al., 2018a; Wen et al., 2018).

The photolysis frequencies of $J(NO_2)$, $J(HONO)$, $J(O^1D)$ were computed with the NCAR Tropospheric Ultraviolet and Visible (TUV) Transfer Model (http://www.acd.ucar.edu/TUV), with the O_3 column density obtained from the Total Ozone Mapping Spectrometer (TOMS, data available at http://toms.gsfc.nasa.gov/teacher/ozone). In spring when the measured $J(NO_2)$ was available, the calculated

J(HONO) and J(O^{1}D) were scaled with the ratio of measured J(NO$_2$) to calculated J(NO$_2$). In winter, without direct observations of J(NO$_2$), the TUV-calculated J values were approximated by multiplying the average ratio of measured J(NO$_2$) to calculated J(NO$_2$) obtained in spring (i.e., 0.7). It should be noted that such estimation of J values is subject to some uncertainties, especially for those in winter when direct J(NO$_2$) measurements were unavailable. Nonetheless, scaling the TUV-calculated clear-sky J values with the same ratio should not alter the major conclusion of this study regarding the impacts of HONO photolysis on the HOx sources and atmospheric oxidation capacity.

2.3 Lagrangian Particle Dispersion Model

A Lagrangian Particle Dispersion Model (WRF-FLEXPART v3.3) was utilized to investigate the provenance and trajectory of the air masses sampled at Mt. Tai. The Weather Research and Forecasting (WRF) Model, driven by the NCEP FNL reanalysis data (https://rda.ucar.edu/datasets/ds083.3/index.html#sfol-fw?g=201608), was run to produce the high spatial resolution meteorological field. The horizontal resolution of the WRF model simulations was 20 km, and the vertical direction was divided into 30 layers under 100 hPa, including 18 layers below the altitude of 2 km. In the LPDM simulations, 3000 particles were released for 3-days backward trajectories from the observational station at the altitude of 1400 m a.g.l. The domain was in the range of 105°E-126°E and 25.5°N-43.5°N with 0.1°× 0.1° grids. The residence time of particles for a thickness 100 m above the surface in all grid cell was calculated as the "footprint" retroplume, which indicated the distribution of probability or residence time of a simulated air mass at the surface level. This method has been widely applied in the previous studies (Stohl et al., 2003; Ding et al., 2009; Pan et al., 2014).

2.4 Chemical box model

A chemical box model was used to simulate the in-situ tropospheric oxidation chemistry and quantify the contributions of HONO to the OH source and atmospheric oxidative capacity. It was set up based on the Master Chemical Mechanisms (MCM, v3.3.1), a nearly explicit chemical mechanism describing the degradation of 143 primary VOC compounds in addition to the latest inorganic reactions (Jenkin et al., 2003; Saunders et al., 2003). The model was constrained with the measured concentrations of NO, NO$_2$, CO, SO$_2$, O$_3$, VOCs and carbonyls as well as the meteorological conditions at a time interval of 5 min. For VOCs and carbonyls for which the measurements were not in real-time, the high-resolution data were approximated as follows. During the daytime when multiple VOC and carbonyl samples were available, the measurement data were interpolated to a time resolution of 5 min. For the period when measurement data were unavailable, the VOC concentrations (except for isoprene) were estimated with the real-time CO data by assuming a linear regression relationship between VOCs and CO (note that the regression was established with the available

measurement data of VOCs and CO). The same method was applied for isoprene and carbonyls, but ambient temperature was used instead of CO for isoprene, and multi-linear regression with CO and O_3 was used for carbonyls to account for the primary and secondary sources of carbonyls (Yang et al., 2018; Xue et al., 2016). Such approximation may be subject to some uncertainties but should not significantly interfere the estimation of the role of HONO photolysis in OH sources (Yang et al., 2018). The model computed the major primary production rates of RO_x radicals (RO_x=OH+HO_2+RO_2), including photolysis of O_3, HONO, HCHO and other OVOCs, and the ozonolysis reactions of unsaturated VOCs (Xue et al., 2016). Also calculated by the model was the AOC by OH, which is defined here as the sum reaction rate of OH with NO, NO_2, SO_2, CO and VOCs (AOC = $\Sigma(k_{OH}[OH][Xi])$: [Xi] is the concentration of the individual reactant species, and K_{OH} is the rate coefficient of OH with Xi). The model simulations were performed for the two campaigns, and a four-day pre-run was made with constraints of campaign-average data to facilitate the model to a chemical steady state for the unconstrained species. Two model scenarios with and without the measured HONO constraints were done to assess the contribution of the unknown HONO sources to the OH chemistry (note that the model only contained the homogeneous source of HONO). This model has been extensively adopted to simulate the radical chemistry and ozone formation in our previous studies (Xue et al., 2014; Xue et al., 2016; Yang et al., 2018).

3 Results and Discussion

3.1 Concentration levels and temporal variations

Table 1 summarizes the statistics of major trace gases, $PM_{2.5}$, and meteorological parameters observed at Mt. Tai during the two campaigns, and the detailed time series of HONO and related species are shown in Figs. S1-S2. The atmospheric conditions at Mt. Tai were dominated by cold and dry weather (especially in winter with average (±standard deviation; SD) temperature and RH of -5.2±3.8 °C and 48±20%) as well as relatively lower concentrations of air pollutants. This was due to the high elevation of the station, which is primarily located in the lower FT and/or upper PBL during the measurement periods. The sampled air masses at Mt. Tai were rather chemically aged, as indicative of the low NO_x/NO_y ratios with average values (±SD) of 0.45±0.21 and 0.25±0.19 in winter and spring, respectively. The average concentrations of NO_x (4.64±3.75 ppbv), SO_2 (3.8±4.2 ppbv), and $PM_{2.5}$ (41.1±28.2 µg/m³) in winter were significantly higher than those in spring (2.18±2.09 ppbv for NO_x, 1.6±1.6 ppbv for SO_2, and 33.7±26.7 µg/m³ for $PM_{2.5}$), while an opposite seasonal pattern was found for O_3 (49±12 ppbv in winter vs 63±14 ppbv in spring). The ambient levels of HONO were comparable in both seasons, with average mixing ratios (±SD) of 0.15±0.15 and 0.13±0.15 ppbv in winter and spring. Despite the relatively low average concentration levels, spikes in HONO (and NO_x, NO_y,

CO and PM$_{2.5}$) concentrations were frequently encountered throughout the measurement periods (see Figs. S1-S2), indicating the transport of polluted plumes to the mountaintop. The maximum HONO mixing ratios were recorded at 1.14 and 3.23 ppbv in winter and spring, respectively. The above inspection of data reveals the overall moderate HONO concentration levels as well as the frequent occurrence of HONO-laden plumes in the upper PBL and lower FT of the NCP region.

Table 2 compares the HONO concentration levels at Mt. Tai with those measured at various surface sites as well as in the high-elevation atmospheres around the world. Obviously, the HONO concentrations at Mt. Tai were significantly lower than those observed at the polluted surface sites in China. For example, the ambient HONO levels at Mt. Tai were approximately an order of magnitude lower than those at urban or suburban sites in the NCP and Pearl River Delta (PRD) regions. This is within expectation considering the height of Mt. Tai and the short lifetime of HONO. A detailed comparison against the measurement results at a nearby urban site will be made in Section 3.2 to infer the vertical distribution of HONO in this region. Despite the lower absolute levels, a noteworthy result is the HONO/NO$_2$ ratios at Mt. Tai (0.059±0.091 in winter and 0.072±0.080 in spring) are well within the reported ranges (0.041-0.093) obtained at these surface sites (Su et al., 2008b; Li et al., 2012; Wang et al., 2017; Li et al., 2018a; Liu et al., 2019), implying that NO$_2$ might be the key factor governing the regional distribution (or formation) of HONO. Another important finding from the comparison is that the HONO concentrations at Mt. Tai are substantially higher than those measured from the high-elevation atmospheres, e.g., Whiteface mountain, U.S. (Zhou et al., 2007), Summit, Greenland (Dibb et al., 2002), Hohenpeissenberg, Germany (Acker et al., 2006), Mt. Brocken, Germany (Acker et al., 2001), and aboard research aircraft over the North Atlantic Ocean (Ye et al., 2016), northern Michigan (Zhang et al., 2009), and southeastern U.S. (Ye et al., 2018). This demonstrates the higher pollution levels of HONO in the upper PBL and lower FT in the NCP region, which may further lead to stronger supply of OH radicals and higher atmospheric oxidation capacity in the high-elevation atmosphere. It is very important to pin down the sources of the elevated HONO and fully evaluate their impacts on OH radicals and AOC in the upper PBL and lower FT of the NCP region, which will be detailed in the following sections.

Figure 2 shows the average diurnal variation patterns of HONO and related parameters during the two measurement campaigns. Overall, most pollutants including NO$_2$, NO$_y$, CO, O$_3$ and PM$_{2.5}$ showed well-defined diurnal profiles with a daytime concentration peak compared to lower levels during the nighttime (note that the exact peak time varied among the individual pollutants with different lifetimes and photochemical behaviors). This can be explained by the evolution of the PBL, mountain-valley breeze, and atmospheric photochemistry (Sun et al., 2016). Similar diurnal patterns were also found for HONO, showing noontime concentration peaks with relatively lower mixing ratios during the night in both seasons. Such

pattern is quite different from those determined by most previous studies at the ground level, which generally show higher nighttime concentrations but with a daytime trough (Lee et al., 2016; Li et al., 2018a; Liu et al., 2019; Fu et al., 2019). The noontime HONO maximum (e.g., ~11:00-15:00 LT) at Mt. Tai suggested the potential upslope transport of HONO to the mountaintop and/or the presence of 'additional' daytime sources. The almost coincident noontime concentration peak of CO (e.g., ~12:00-15:00 LT) confirmed the upslope transport of boundary layer air to the mountaintop. We also examined the diurnal variations of $HONO/NO_2$, the ratio commonly used to indicate the efficiency of HONO formation from the reactions involving NO_2 (Yu et al., 2009). From Fig. 2c, the $HONO/NO_2$ ratio shows an increasing trend throughout the nighttime together with an extra peak during the midday in both seasons. This indicates the nighttime HONO formation and accumulation from the heterogeneous reactions of NO_2 as well as the presence of some 'additional' daytime sources. The higher daytime $HONO/NO_2$ ratios in spring than in winter suggest the action of photo-enhanced heterogeneous formation of HONO. The daytime HONO sources will be diagnosed via a detailed PSS calculation in Section 3.3.

3.2 Potential transport by PBL evolution and mountain-valley breeze

In this section, we compare our observations at Mt. Tai with the recent year-round measurement results obtained at a surface site in Ji'nan to infer the vertical gradient of HONO over the NCP region, and examine the vertical transport of HONO with the LPDM modeling. The surface site is located in the downtown of Ji'nan city, which is about 60 km to the north of Mt. Tai (Fig. 1), and the measurement data have been reported by Li et al. (2018a). It should be noticed that both measurements were not conducted at the same time, and only the average conditions of HONO and NO_2 in the same season were compared here.

Figure 3 presents the average diurnal variations of HONO, NO_2, and $HONO/NO_2$ at both surface and mountaintop in winter and spring. Several interesting aspects are clearly illustrated from the figure. First, the diurnal variation patterns are distinct between at surface and at the mountaintop. HONO showed higher concentrations at nighttime and lower levels during the day at surface, which is opposite to the profile at the mountaintop. Second, the HONO and NO_2 concentrations at surface were overall almost an order of magnitude higher than those at Mt. Tai, but the vertical gradient (as indicative of the Mountaintop/Surface (M/S) concentration ratio) showed a clear diurnal dependence. The M/S ratios of HONO at nighttime (18:00-6:00 LT; with averages of 0.05±0.01 and 0.07±0.02 in winter and spring, respectively) were significantly lower than those during the midday (11:00-15:00 LT; 0.28±0.04 and 0.23±0.03). This is also the case for NO_2, and should be ascribed to the efficient mixing within the PBL and upslope transport driven by the valley breeze during the daytime. Third, although the $HONO/NO_2$ ratios were almost comparable at both surface and Mt.

Tai during the night, the daytime ratios were significantly higher at the mountaintop (0.065±0.093 and 0.093±0.094) than at the surface (0.047±0.090 and 0.052±0.040). It implies the enhanced HONO formation from the NO_2-involved sources at the mountaintop, especially in spring (see Fig. 3).

Can the PBL mixing and mountain-valley breeze transport HONO from the ground level to the mountaintop with an altitude of ~1.5 km, given its quite short lifetime? The vertical transport distance (σ) driven by the turbulent diffusion can be estimated by the following equation (E2) [Jacob, 1999].

$$\sigma=(2K_Z\tau_{HONO})^{1/2} \qquad\qquad (E2)$$

Where, Kz is the turbulent diffusion coefficient, and τ_{HONO} is the chemical lifetime of HONO. In the early morning when the boundary layer is stable, Kz is usually within the range of $10^2 \sim 10^5$ cm^2 s^{-1} and increases with the temperature (Zhang et al., 2009). Assuming an overall τ_{HONO} of 60 minutes in the early morning (corresponding to a J(HONO) of 2.8×10^{-4} s^{-1}), the vertical transport distance of the ground-level HONO is estimated in the range of 9-268 m, far below the altitude of Mt. Tai. This explains the huge difference in the HONO concentrations between the surface site and the mountaintop in the early morning and during the nighttime. Around noontime, the PBL has been developed and K_Z is generally in the order of 10^6 cm^2 s^{-1} (Zhang et al., 2009). Adopting a median value of Kz (5×10^6 cm^2 s^{-1}) and τ_{HONO} (25 minutes; refer to Section 3.3 for the lifetime estimation), the maximum transport distance of HONO can be up to 1200 m, which is still below the peak of Mt. Tai. If we further consider the mountain-valley breeze, by adopting a mean upslope wind speed of 1 m/s (Kalthoff et al., 2000; Wang et al., 2015), the transport height of HONO by the valley breeze is estimated to be 1500 m. Note that the transported HONO from the ground level may be subject to extensive dilution and more photolysis at higher altitudes. Therefore, the PBL evolution and valley breeze should play an important role in the regional transport of HONO in the mountainous areas.

The LPDM modelling results also support the upslope transport of surface pollution to the Mt. Tai. Figure 4 shows the average distributions of the "footprint" retroplume of the three-day backward trajectories, computed by the WRF-FLEXPART model, arriving at Mt. Tai during both daytime and nighttime. During the night and early morning (2:00-8:00 LT), obviously, the air masses sampled at Mt. Tai were mainly originated from long-range transport and less affected by the PBL air from the NCP region (Fig. 4a and 4c). This can be explained by that Mt. Tai is in the free troposphere (or residual layer) and under the influence of downslope mountain breeze during the nighttime. In comparison, the air masses reaching Mt. Tai in the afternoon (12:00-18:00 LT) primarily came from the boundary layer in the nearby regions (i.e., Ji'nan, Tai'an and Ji'ning, major cities surrounding Mt. Tai; Figs 4b and 4d). Note that the "footprint" retroplume denotes the residence time of particles within the lowest 100 m near surface. This demonstrates the efficient transport of regional surface

air pollution to the mountaintop with the development of PBL and valley breeze.

3.3 Daytime HONO sources

Exploration of the potential daytime source has been a major objective of the recent HONO observational studies. Here we diagnose the possible daytime sources of HONO in the upper PBL and lower FT by performing a PSS analysis for the measurement data collected at Mt. Tai. According to the measurement-derived J(HONO) (with noontime averages of 6.4 ± 3.5 and $9.5\pm3.2\times10^{-4}$ s^{-1} in winter and spring; see Fig. S3) and the model-simulated OH concentrations (with noontime averages of 2.5 ± 0.7 and $4.4\pm2.0\times10^{6}$ molecules cm^{-3}; Fig. S3), the average lifetime of HONO was estimated as 25.7 ± 1.4 and 21.8 ± 16.9 minutes during noontime (11:00-14:00 LT) in winter and spring, respectively. Given such short lifetimes, the air masses arriving at Mt. Tai at noon should facilitate a steady state for HONO. The PSS concentrations of HONO ([HONO]$_{pss}$) can be deduced from Equation (E1), if we only took the homogeneous formation from OH+NO reactions, HONO photolysis, and OH+HONO reactions into account. Note that the OH concentrations were simulated with the observation-constrained MCM model as described in Section 2.4 (see Fig. S3 for detailed time series of OH). The PSS approach has been widely used in the previous studies (Zhou et al., 2002; Kleffmann et al., 2005; Elshorbany et al., 2012).

Figure 5 shows the campaign-average [HONO]$_{pss}$ at noontime and the comparison with the measured HONO concentrations in the two seasons. It is evident that the [HONO]$_{pss}$ was significantly lower than the measured data. On average, [HONO]$_{pss}$ only accounted for 18% and 12% of the ambient HONO levels at Mt. Tai in winter and spring (see Fig. S4), demonstrating the existence of strong HONO sources other than the homogeneous OH+NO reactions. To maintain the observed HONO levels, an additional 'source' is needed and its source strength (hereafter referred to as P$_{other}$) can be calculated from Equation (E3).

$$P_{other} = [HONO]_{obs}\times J(HONO)+ [HONO]_{obs}\times[OH]\times K_{OH+HONO}-[NO]\times[OH]\times K_{OH+NO} \quad (E3)$$

In the present study, the P$_{other}$ was calculated in the range of 0.01-1.24 and 0.01-4.26 ppb/h, with average ($\pm$SD) values of 0.45 ± 0.25 and 0.64 ± 0.49 ppb/h in winter and spring, respectively. In comparison, the noontime HONO production rates from the OH+NO reactions were 0.13 ± 0.10 and 0.09 ± 0.08 ppb/h, much lower than P$_{other}$. The additional source strengths of daytime HONO at Mt. Tai are much lower than those previously reported at the surface sites in Ji'nan (2.95 ppb/h; Li et al., 2018a), Beijing (1.83 ppb/h; Hou et al., 2016), and Santiago, Chile (1.69 ppb/h; Elshorbany et al., 2009), and are comparable to those derived from the rural or mountain sites, such as Hohenpeissenberg (0.40 ppb/h; Acker et al., 2006), Whiteface mountain (0.38 ppb/h; Zhou et al., 2007), and a forest site in Julich, Germany (0.50 ppb/h; Kleffmann et al., 2005). Some studies

have reported much lower P_{other} values obtained from aircraft studies in Michigan (0.057 ppb/h; Zhang et al., 2009) and in Southern US (0.17 ppb/h; Ye et al., 2018).

Recent field and laboratory studies have proposed some potential sources that may help explain the observed higher-than-PSS daytime HONO levels. Among them, direct emissions from vehicle exhaust and soil microbiological processes, heterogeneous conversion of NO_2 to HONO on surfaces, and photolysis of adsorbed and aqueous-phase nitrate are relatively well received to be relevant in the ambient atmospheres (Zhou et al., 2003; Su et al., 2011; VandenBoer et al., 2013; Liu et al., 2019). It is believed that vehicle and soil emissions should be of minor importance at Mt. Tai, which is free from anthropogenic activities and soil surfaces. We then diagnosed the potential action of heterogeneous formation of HONO on both ground and aerosol surfaces as well as photolysis of nitrate, by examining the relationship between P_{other} and a variety of indicators for the specific HONO sources. Such correlation analysis method has been widely applied in many previous studies to identify the most likely additional daytime HONO source, despite the inherent uncertainty in the statistical approach (Su et al., 2008b; Lee et al., 2016; Lu et al., 2018).

Figure 6 shows the scatter plots of P_{other} against several HONO source indicators during the two campaigns. As illustrated from the figure, P_{other} shows weak correlation with NO_2 (the commonly used indicator for the heterogeneous NO_2-to-HONO conversion on the ground surface, by assuming that the ground surface density is uniform in the PBL), with correlation coefficients (r) of 0.26 and 0.24 in winter and spring, respectively. This indicates that the heterogeneous reactions on the ground should not be the dominant HONO source at Mt. Tai. If the aerosol surface area density ($(S/V)_a$) was included, the correlations were significantly improved (Figs. 6b and 6e), with r values of 0.52 and 0.43 between P_{other} and $NO_2*(S/V)_a$ (an indicator of the heterogeneous NO_2-to-HONO conversion on aerosol surface). Furthermore, the correlations were further improved after $J(NO_2)$ (an indicator of sunlight) was considered, with the r being 0.54 and 0.48 for P_{other} versus $J(NO_2)* NO_2*(S/V)_a$ (Figs. 6c and 6f). These results suggest that the photo-enhanced heterogeneous reactions of NO_2 on the aerosol surface should be a significant daytime HONO source at Mt. Tai. This is different from most previous studies conducted at the ground level showing the dominant role of ground surface in the heterogeneous HONO formation (Kleffmann et al., 2003; Su et al., 2008a; Xu et al., 2015; Li et al., 2018a), and highlights the importance of aerosol surface in the HONO formation in the upper PBL and lower FT. Besides, Fig. S5 shows the relatively weak correlation between P_{other} and $J(NO_2)*pNO_3^-$ (the indicator for the photolysis of particulate nitrate), with r of 0.17 and 0.03, indicating the nitrate photolysis is relatively insignificant to the ambient HONO at Mt. Tai.

Possibility of measurement interference from peroxynitric acid (PNA; HO_2NO_2): While the LOPAP

instrument has been extensively tested for a variety of interferences (Heland et al., 2001; Kleffmann and Wiesen, 2008), some recent studies reported that it may be subject to positive interference from HO_2NO_2 (e.g., Legrand et al., 2014). Due to the thermal instability of HO_2NO_2, its interference is generally negligible at ambient temperatures at the ground level, but may become important in the circumstances with low temperature and active photochemistry. Legrand et al. (2014) reported that the interference from HO_2NO_2 to their HONO measurements was about 15% according to laboratory experiments. In the present study, we did not conduct in-situ measurements of HO_2NO_2. To estimate the potential interference for our HONO measurements, we simulated the HO_2NO_2 concentrations at Mt. Tai in both campaigns by the MCM chemical box model constrained with all measured species including HONO. Figure S6 shows the time series of modelled HO_2NO_2 and its comparison with the measured HONO and missing HONO (measured HONO minus $[HONO]_{pss}$) concentrations. Overall, moderate concentration levels of HO_2NO_2 were predicted by the model at Mt. Tai, with average values (±SD) of 0.07±0.06 ppbv and 0.03±0.04 ppbv in winter and spring, respectively. If we took the HO_2NO_2 interference of 15% (Legrand et al., 2014), the potential interference to the missing HONO were 16%±15% and 11%±10% in winter and spring, respectively. Figure S7 shows the scatter plots of missing HONO versus $[NO_2]*J(NO_2)$, an indicator of the HO_2NO_2 production. As we can see, the correlation was rather weak between missing HONO and $[NO_2]*J(NO_2)$, especially in winter (r=0.19). This indicates that the interference from HO_2NO_2 may not be a major factor in the determined missing HONO, and more experiments are needed to confirm and quantify the possible interferences to the ambient HONO observations.

3.4 Impacts of HONO on OH radical and atmospheric oxidation capacity

The detailed chemical budget of RO_x radicals was explored by the observation-based MCM box model. Figure 7 shows the average diurnal profiles of primary production rates of OH, HO_2 and RO_2 radicals from major sources at Mt. Tai during the two campaigns, and the statistical results are documented in Table 3. Two points are noteworthy here. First, the primary production rates of RO_x radicals at Mt. Tai were substantially lower than those derived from most of the ground-level sites over China, such as Beijing (Liu et al., 2012; Yang et al., 2018), Wuhan (Lu et al., 2017), Chengdu (Tan et al., 2018), Hong Kong (Xue et al., 2016; Li et al., 2018b), and a rural site in the Yellow River Delta region (Chen et al., 2020). Note that most of these previous studies were based on modelling of the polluted photochemical episodes, but the modelled highest RO_x production rates at Mt. Tai were still lower than these studies. The model-simulated daily maximum AOC (defined here as the sum of reaction rates of OH with NO_x, SO_2, CO and VOCs) at Mt. Tai was in the range of 1.3-3.9×10^7 and 0.6-10.8×10^7 molecules cm^{-3} s^{-1} in winter and spring (see Fig. S8), respectively, which are still much lower than those at the abovementioned surface sites (Xue et al., 2016; Yang et al., 2018; Li et al.,

2018b). This demonstrates the relatively lower oxidation capacity of the upper PBL and lower FT atmosphere compared to the polluted surface-layer air. Nonetheless, the primary RO_x production rates at Mt. Tai were comparable to those obtained from Hohenpeissenberg, Germany (Acker et al., 2006), Whiteface mountain (Zhou et al., 2007), and Pinnacle State Park, a rural site in southwestern New York (Zhou et al., 2002).

Second, photolysis of HONO presents the predominant primary OH source, and is also among the most important sources of RO_x at Mt. Tai. In winter, HONO photolysis was the overwhelming primary source of RO_x radicals, with the mid-day (9:00-15:00 LT) average production rate 0.520 ppb/h, followed by photolysis of OVOCs other than formaldehyde (0.210 ppb/h for HO_2 and 0.182 ppb/h for RO_2) and formaldehyde (0.193 ppb/h for HO_2), ozonolysis reactions of unsaturated VOCs (0.036 ppb/h for RO_x), and O_3 photolysis (0.022 ppb/h for OH). In spring, in comparison, photolysis of OVOCs other than formaldehyde turns over to be the dominant RO_x source (with mid-day average rate of 0.434 ppb/h for HO_2 and 0.407 ppb/h for RO_2), then photolysis of HONO (0.511 ppb/h for OH), formaldehyde (0.374 ppb/h for HO_2) and O_3 (0.178 ppb/h for OH), and reactions of O_3+VOCs (0.057 ppb/h for RO_x). In percentage, HONO photolysis accounted for 44.4% and 25.8% of the total primary RO_x production at mid-day at Mt. Tai in winter and spring, respectively. For OH alone, the percentages of the contribution of HONO photolysis to the primary sources were 93.2% and 71.3% in winter and spring. Evidently, HONO photolysis plays a very important role in the OH supply and hence jump-start of atmospheric oxidation chemistry in the upper PBL and lower FT in the NCP region.

How much do the additional HONO sources (other than the homogeneous OH+NO source) affect the atmospheric photochemistry in the upper PBL and lower FT? To evaluate this issue, two modelling scenarios were performed, with and without constraints of the measured HONO data. The model only contains the homogeneous HONO formation from OH+NO reaction, and thus the difference between both scenarios can represent the effects of the additional daytime HONO sources. Figure 8 documents the differences in the model-simulated OH, HO_2, AOC, and P_{OH} (primary production rate of OH) between the two scenarios in winter and spring. Clearly, the model only considering the homogeneous source and without observational constraints predicted much lower levels of the HO_x radicals and AOC at Mt. Tai. Specifically, the discrepancy in the mid-day (9:00-15:00) average P_{OH}, OH, HO_2, and AOC can be up to 83.4% (63.7%), 47.2% (27.1%), 39.7% (20.3%), and 46.1% (26.4%) in winter (spring), compared to the base scenario with constraints of the measured HONO data. Given the essential role of HO_x radicals in the atmospheric chemistry, the models would largely underestimate the atmospheric oxidation processes in the upper PBL and lower FT, if the measurement data and/or additional HONO source mechanisms were absence. So far, direct observations of HONO in the high-elevation atmospheres are still lacking, and accurate representation of the HONO sources in atmospheric chemistry models is underway. This study highlights the significance of HONO chemistry in

the upper PBL and lower FT in the NCP region, and calls on more efforts to address the tempo-spatial variations and sources of HONO in the high-elevation atmospheres.

4. Conclusions

We analyzed the characteristics, sources, and impacts on tropospheric oxidation chemistry of ambient HONO in the upper PBL and lower FT of the NCP region, by conducting intensive field observations at Mt. Tai (the peak of the region) followed by detailed modelling analyses. Moderate concentration levels of HONO were observed, which are higher than those measured from other high-elevation areas around the world. HONO showed a distinctive diurnal variation pattern at Mt. Tai with a daytime concentration peak compared to lower levels at night, which is opposite to the results determined at the ground level. The evolution of PBL and the upslope transport driven by valley breezes explained the observed daytime HONO peak. The data were compared with the year-round continuous measurement results at a nearby surface urban site to infer the vertical gradient of HONO in the NCP region. Strong additional daytime HONO sources other than homogeneous OH+NO reactions existed in the PBL, and the PSS estimation only accounted for 18% and 12% of the observed HONO in winter and spring. The photo-enhanced heterogeneous reactions of NO_2 on aerosol surface appears to be an important HONO source. HONO photolysis is the predominant primary source of OH radical, and plays a major role in the radical chemistry at Mt. Tai. With only inclusion of the OH+NO reactions, significant reductions of the modelled OH (by ~47.2%; 27.1%), HO_2 (by ~39.7%; 20.3%), P_{OH} (by ~83.4%; 63.7%), and AOC (by ~46.1%; 26.4%) were found, compared with being constrained by observed HONO data. This study elucidates the significant role of HONO in the atmospheric oxidation chemistry in the upper PBL and lower FT of the NCP region, where previous studies mainly focused on HONO at the ground level.

Acknowledgements

The authors thank all the staff of the Taishan National Reference Climatological Station for their logistics and help during the field observations. We are grateful for the MCM group of the Leeds University for provision of the MCM model. This work was sponsored by the National Key Research and Development Program of China (2016YFC0200500), National Natural Science Foundation of China (41922051 and 91544213), Shandong Provincial Science Foundation for Distinguished Young Scholars (ZR2019JQ09), the Jiangsu Collaborative Innovation Center for Climate Change, and the Taishan Scholars (ts201712003). We thank the three anonymous referees whose comments are very helpful for improving the original manuscript.

Data availability

The measurement data and model output used in the present study can be accessed from https://data.mendeley.com/datasets/wcn84cybx9/draft#folder-defadc56-944c-4f33-af54-14019d73ac61. The code for the MCM model can be downloaded from the MCM website (http://mcm.leeds.ac.uk/MCMv3.3.1/home.htt).

References

Acker, K., Möller, D., Wieprecht, W., Auel, R., Kalaß, D., and Tscherwenka, W.: Nitrous and nitric acid measurements inside and outside of clouds at Mt. Brocken, Water, Air, Soil Pollut., 130, 331-336, 2001.

Acker, K., Möller, D., Wieprecht, W., Meixner, F. X., Bohn, B., Gilge, S., Plass-Dülmer, C., and Berresheim, H.: Strong daytime production of OH from HNO$_2$ at a rural mountain site, Geophys. Res. Lett., 33, L02809, 2006.

Alicke, B., Geyer, A., Hofzumahaus, A., Holland, F., Konrad, S., Pätz, H., Schäfer, J., Stutz, J., Volz-Thomas, A., and Platt, U.: OH formation by HONO photolysis during the BERLIOZ experiment, J. Geophys. Res.: Atmos., 108, PHO 3-1-PHO 3-17, 2003.

Baergen, A. M. and Donaldson, D. J.: Formation of reactive nitrogen oxides from urban grime photochemistry, Atmos. Chem. Phys., 16, 6355–6363, 2016.

Bejan, I., Abd El Aal, Y., Barnes, I., Benter, T., Bohn, B., Wiesen, P., and Kleffmann, J. r.: The photolysis of ortho-nitrophenols: a new gas phase source of HONO, Phys. Chem. Chem. Phys., 8, 2028-2035, 2006.

Colussi, A. J., Enami, S., Yabushita, A., Hoffmann, M. R., Liu, W. G., Mishra, H., and Goddard, W. A.: Tropospheric Aerosol as Reactive Intermediate, Faraday Discuss., 165, 407-420, 2013.

Cui, L., Li, R., Zhang, Y., Meng, Y., Fu, H., and Chen, J.: An observational study of nitrous acid (HONO) in Shanghai, China: The aerosol impact on HONO formation during the haze episodes, Sci. Total Environ, 630, 1057-1070, 2018.

Chen, T., Xue, L., Zheng, P., Zhang, Y., Liu, Y., Sun, J., Han, G., Li, H., Zhang, X., Li, Y., Li, H., Dong, C., Xu, F., Zhang, Q., and Wang, W.: Volatile organic compounds and ozone air pollution in an oil production region in northern China, Atmos. Chem. Phys., 20, 7069–7086, 2020.

Dibb, J. E., Arsenault, M., Peterson, M. C., and Honrath, R. E.: Fast nitrogen oxide photochemistry in Summit, Greenland snow, Atmos. Environ., 36, 2501-2511, 2002.

Ding, A., Wang, T., Xue, L., Gao, J., Stohl, A., Lei, H., Jin, D., Ren, Y., Wang, X., and Wei, X.: Transport of north China air pollution by midlatitude cyclones: Case study of aircraft measurements in summer 2007, J. Geophys. Res.: Atmos., 114 (D8), D08304, 2009.

Elshorbany, Y. F., Kurtenbach, R., Wiesen, P., Lissi, E., Rubio, M., Villena, G., Gramsch, E., Rickard, A., Pilling, M., and Kleffmann, J.: Oxidation capacity of the city air of Santiago, Chile, Atmos. Chem. Phys., 9, 2257-2273, 2009.

Elshorbany, Y. F., Steil, B., Bruhl, C., and Lelieveld, J.: Impact of HONO on global atmospheric chemistry calculated with an empirical parameterization in the EMAC model, Atmos. Chem. Phys., 12, 9977-10000, 2012.

Fu, X., Wang, T., Zhang, L., Li, Q., Wang, Z., Xia, M., Yun, H., Wang, W., Yu, C., and Yue, D.: The significant contribution of HONO to secondary pollutants during a severe winter pollution event in southern China, Atmos. Chem. Phys., 2019.

Gao, J., Wang, T., Ding, A., and Liu, C.: Observational study of ozone and carbon monoxide at the summit of mount Tai (1534 m asl) in central-eastern China, Atmos. Environ., 39, 4779-4791, 2005.

Heland, J., Kleffmann, J., Kurtenbach, R., and Wiesen, P.: A new instrument to measure gaseous nitrous acid (HONO) in the atmosphere, Environ. Sci. Technol., 35, 3207-3212, 2001.

Hou, S., Tong, S., Ge, M., and An, J.: Comparison of atmospheric nitrous acid during severe haze and clean periods in Beijing, China, Atmos. Environ., 124, 199-206, 2016.

Jacob, D. J.: Introduction to atmospheric chemistry, Princeton University Press, 1999.

Jenkin, M., Saunders, S., Wagner, V., and Pilling, M.: Protocol for the development of the Master Chemical Mechanism,

MCM v3 (Part B): tropospheric degradation of aromatic volatile organic compounds, Atmos. Chem. Phys., 3, 181-193, 2003.

Kalthoff, N., Horlacher, V., Corsmeier, U., Volz-Thomas, A., Kolahgar, B., Geiß, H., Möllmann-Coers, M., and Knaps, A.: Influence of valley winds on transport and dispersion of airborne pollutants in the Freiburg-Schauinsland area, J. Geophys. Res.: Atmos., 105, 1585-1597, 2000.

Kleffmann, J., Kurtenbach, R., Lörzer, J., Wiesen, P., Kalthoff, N., Vogel, B., and Vogel, H.: Measured and simulated vertical profiles of nitrous acid—Part I: Field measurements, Atmos. Environ., 37, 2949-2955, 2003.

Kleffmann, J., Gavriloaiei, T., Hofzumahaus, A., Holland, F., Koppmann, R., Rupp, L., Schlosser, E., Siese, M., and Wahner, A.: Daytime formation of nitrous acid: A major source of OH radicals in a forest, Geophys. Res. Lett., 32 (5), L05818, 2005.

Kleffmann, J., and Wiesen, P.: Technical Note: Quantification of interferences of wet chemical HONO LOPAP measurements under simulated polar conditions, Atmos. Chem. Phys., 8, 6813-6822, 2008.

Kukui, A., Legrand, M., Preunkert, S., Frey, M. M., Loisil, R., Roca, J. G., Jourdain, B., King, M. D., France, J. L., and Ancellet, G.: Measurements of OH and RO_2 radicals at Dome C, East Antarctica, Atmos. Chem. Phys., 14, 12373-12392, 2014.

Lee, J., Whalley, L., Heard, D., Stone, D., Dunmore, R., Hamilton, J., Young, D., Allan, J., Laufs, S., and Kleffmann, J.: Detailed budget analysis of HONO in central London reveals a missing daytime source, Atmos. Chem. Phys., 16, 2747-2764, 2016.

Legrand, M., Preunkert, S., Frey, M., Bartels-Rausch, T., Kukui, A., King, M. D., Savarino, J., Kerbrat, M., and Jourdain, B.: Large mixing ratios of atmospheric nitrous acid (HONO) at Concordia (East Antarctic Plateau) in summer: a strong source from surface snow?, Atmos. Chem. Phys., 14, 9963-9976, 2014.

Li, D., Xue, L., Wen, L., Wang, X., Chen, T., Mellouki, A., Chen, J., and Wang, W.: Characteristics and sources of nitrous acid in an urban atmosphere of northern China: results from 1-yr continuous observations, Atmos. Environ., 182, 296-306,, 2018a.

Li, X., Brauers, T., Häseler, R., Bohn, B., Hofzumahaus, A., Holland, F., Lu, K., Rohrer, F., Hu, M., and Zeng, L.: Exploring the atmospheric chemistry of nitrous acid (HONO) at a rural site in Southern China, Atmos. Chem. Phys., 12, 1497-1513, 2012.

Li, X., Holland, F., Wahner, A., Wolfe, G., Wegener, R., Hofzumahaus, A., Rohrer, F., Mentel, T. F., Brauers, T., and Bohn, B.: Missing gas-phase source of HONO inferred from Zeppelin measurements in the troposphere, Science, 348, 292-296, 2014.

Li, Z., Xue, L., Yang, X., Zha, Q., Tham, Y. J., Yan, C., Louie, P. K., Luk, C. W., Wang, T., and Wang, W.: Oxidizing capacity of the rural atmosphere in Hong Kong, Southern China, Sci. Total Environ., 612, 1114-1122, 2018b.

Liu, Y., Lu, K., Li, X., Dong, H., Tan, Z., Wang, H., Zou, Q., Wu, Y., Zeng, L., and Hu, M.: A comprehensive model test of the HONO sources constrained to field measurements at rural North China Plain, Environ. Sci. Technol., 53, 3517-3525, 2019.

Liu, Z., Wang, Y., Gu, D., Zhao, C., Huey, L., Stickel, R., Liao, J., Shao, M., Zhu, T., and Zeng, L.: Summertime photochemistry during CAREBeijing-2007: RO_x budgets and O_3 formation, Atmos. Chem. Phys., 12, 7737, 2012.

Liu, Z., Wang, Y., Costabile, F., Amoroso, A., Zhao, C., Huey, L. G., Stickel, R., Liao, J., and Zhu, T.: Evidence of aerosols as a media for rapid daytime HONO production over China, Environ. Sci. Technol., 48, 14386-14391, 2014.

Lu, X., Chen, N., Wang, Y., Cao, W., Zhu, B., Yao, T., Fung, J. C., and Lau, A. K.: Radical budget and ozone chemistry during autumn in the atmosphere of an urban site in central China, J. Geophys. Res.: Atmos., 122, 3672-3685, 2017.

Lu, X., Wang, Y., Li, J., Shen, L., and Fung, J. C.: Evidence of heterogeneous HONO formation from aerosols and the regional photochemical impact of this HONO source, Environ. Res. Lett., 13, 114002, 2018.

Monge M E, D'Anna B, Mazri. L.: Light changes the atmospheric reactivity of soot, Proc. Natl Acad. Sci. U. S. A., 107, 6605-6609, 2010.

Michoud, V., Colomb, A., Borbon, A., Miet, K., Beekmann, M., Camredon, M., Aumont, B., Perrier, S., Zapf, P., and Siour, G.: Study of the unknown HONO daytime source at a European suburban site during the MEGAPOLI summer and winter field campaigns, Atmos. Chem. Phys., 14, 2805-2822, 2014.

Nie, W., Ding, A. J., Xie, Y. N., Xu, Z., Mao, H., Kerminen, V.-M., Zheng, L. F., Qi, X. M., Huang, X., and Yang, X.-Q.: Influence of biomass burning plumes on HONO chemistry in eastern China, Atmos. Chem. Phys., 15, 1147-1159, 2015.

Pan, X., Kanaya, Y., Wang, Z., Tang, X., Takigawa, M., Pakpong, P., Taketani, F., and Akimoto, H.: Using Bayesian optimization method and FLEXPART tracer model to evaluate CO emission in East China in springtime, Environ. Sci. Pollut. R., 21, 3873-3879, 2014.

Platt, U., Perner, D., Harris, G., Winer, A., and Pitts, J. j.: Observations of nitrous acid in an urban atmosphere by differential optical absorption, Nature, 285, 312-314, 1980.

Qin, M., Xie, P., Su, H., Gu, J., Peng, F., Li, S., Zeng, L., Liu, J., Liu, W., and Zhang, Y.: An observational study of the HONO–NO_2 coupling at an urban site in Guangzhou City, South China, Atmos. Environ., 43, 5731-5742, 2009.

Saunders, S. M., Jenkin, M. E., Derwent, R., and Pilling, M.: Protocol for the development of the Master Chemical Mechanism, MCM v3 (Part A): tropospheric degradation of non-aromatic volatile organic compounds, Atmos. Chem. Phys., 3, 161-180, 2003.

Simpson, I. J., Blake, N. J., Barletta, B., Diskin, G. S., Fuelberg, H. E., Gorham, K., Huey, L. G., Meinardi, S., Rowland, F. S., and Vay, S. A.: Characterization of trace gases measured over Alberta oil sands mining operations: 76 speciated C2– C10 volatile organic compounds (VOCs), CO_2, CH_4, CO, NO, NO_2, NO_y, O_3 and SO_2, Atmos. Chem. Phys., 10, 11931-11954, 2010.

Sleiman, M., Gundel, L. A., Pankow, J. F., Jacob, P., and Destaillats, H.: Formation of carcinogens indoors by surface-mediated reactions of nicotine with nitrous acid, leading to potential thirdhand smoke hazards, Proc. Natl. Acad. Sci. U. S. A., 107, 6576-6581, 2010.

Sörgel, M., Trebs, I., Wu, D., and Held, A.: A comparison of measured HONO uptake and release with calculated source strengths in a heterogeneous forest environment, Atmos. Chem. Phys., 15, 9237–9251, 2015.

Stohl, A., Forster, C., Eckhardt, S., Spichtinger, N., Huntrieser, H., Heland, J., Schlager, H., Wilhelm, S., Arnold, F., and Cooper, O.: A backward modeling study of intercontinental pollution transport using aircraft measurements, J. Geophys. Res.: Atmos., 108, 2003.

Su, H., Cheng, Y. F., Cheng, P., Zhang, Y. H., Dong, S., Zeng, L. M., Wang, X., Slanina, J., Shao, M., and Wiedensohler, A.: Observation of nighttime nitrous acid (HONO) formation at a non-urban site during PRIDE-PRD2004 in China, Atmos. Environ., 42, 6219-6232, 2008a.

Su, H., Cheng, Y. F., Shao, M., Gao, D. F., Yu, Z. Y., Zeng, L. M., Slanina, J., Zhang, Y. H., and Wiedensohler, A.: Nitrous acid (HONO) and its daytime sources at a rural site during the 2004 PRIDE-PRD experiment in China, J. Geophys. Res.: Atmos., 113, D14312, 2008b.

Su, H., Cheng, Y., Oswald, R., Behrendt, T., Trebs, I., Meixner, F. X., Andreae, M. O., Cheng, P., Zhang, Y., and Poschl, U.: Soil nitrite as a source of atmospheric HONO and OH radicals, Science, 333, 1616-1618, 2011.

Sun, L., Xue, L., Wang, T., Gao, J., Ding, A., Cooper, O. R., Lin, M., Xu, P., Wang, Z., and Wang, X.: Significant increase of summertime ozone at Mount Tai in Central Eastern China, Atmos. Chem. Phys, 16, 10637-10650, 2016.

Tan, Z., Lu, K., Jiang, M., Su, R., Dong, H., Zeng, L., Xie, S., Tan, Q., and Zhang, Y.: Exploring ozone pollution in Chengdu, southwestern China: a case study from radical chemistry to O_3-VOC-NO_x sensitivity, Sci. Total Environ., 636, 775-786, 2018.

Tong, S., Hou, S., Zhang, Y., Chu, B., Liu, Y., He, H., Zhao, P., and Ge, M.: Exploring the nitrous acid (HONO) formation mechanism in winter Beijing: direct emissions and heterogeneous production in urban and suburban areas, Faraday Discuss., 189, 213-230, 2016.

VandenBoer, T. C., Brown, S. S., Murphy, J. G., Keene, W. C., Young, C. J., Pszenny, A., Kim, S., Warneke, C., de Gouw, J. A., Maben, J. R, Wagner, N. L., Riedel T. P., Thornton, J. A., Wolfe, D. E., Dubé, W. P., Öztürk, F., Brock, C. A., Grossberg, N., Lefer, B., Lerner, B., Middlebrook, A. M., and Roberts, J. M.: Understanding the role of the ground surface in HONO

vertical structure: high resolution vertical profiles during NACHTT-11, J. Geophys. Res.: Atmos., 118 (17), 10155-10171, 2013.

Villena, G., Kleffmann, J., Kurtenbach, R., Wiesen, P., Lissi, E., Rubio, M. A., Croxatto, G., and Rappenglück, B.: Vertical gradients of HONO, NO$_x$ and O$_3$ in Santiago de Chile, Atmos. Environ., 45, 3867-3873, 2011.

5   Wang, J., Zhang, X., Guo, J., Wang, Z., and Zhang, M.: Observation of nitrous acid (HONO) in Beijing, China: seasonal variation, nocturnal formation and daytime budget, Sci. Total Environ., 587, 350-359, 2017.

Wang, X., Wang, C., and Li, Q.: Wind regimes above and below a temperate deciduous forest canopy in complex terrain: interactions between slope and valley winds, Atmosphere, 6, 60-87, 2015.

Wen, L., Xue, L., Wang, X., Xu, C., Chen, T., Yang, L., Wang, T., Zhang, Q., and Wang, W.: Summertime fine particulate
10   nitrate pollution in the North China Plain: increasing trends, formation mechanisms and implications for control policy, Atmos. Chem. Phys., 18, 11261-11275, 2018.

Wen, L., Chen, T., Zheng, P., Wu, L., Wang, X., Mellouki, A., Xue, L., and Wang, W.: Nitrous acid in marine boundary layer over eastern Bohai Sea, China: characteristics, sources, and implications, Sci. Total Environ., 670, 282-291, 2019.

Wong, K., Tsai, C., Lefer, B., Haman, C., Grossberg, N., Brune, W. H., Ren, X., Luke, W., and Stutz, J.: Daytime HONO
15   vertical gradients during SHARP 2009 in Houston, TX, Atmos. Chem. Phys., 12, 635-652, 2012.

Xu, Z., Wang, T., Wu, J., Xue, L., Chan, J., Zha, Q., Zhou, S., Louie, P. K., and Luk, C. W.: Nitrous acid (HONO) in a polluted subtropical atmosphere: seasonal variability, direct vehicle emissions and heterogeneous production at ground surface, Atmos. Environ., 106, 100-109, 2015.

Xue, L., Wang, T., Gao, J., Ding, A., Zhou, X., Blake, D., Wang, X., Saunders, S., Fan, S., and Zuo, H.: Ground-level ozone
20   in four Chinese cities: precursors, regional transport and heterogeneous processes, Atmos. Chem. Phys., 14, 13175-13188, 2014.

Xue, L., Gu, R., Wang, T., Wang, X., Saunders, S., Blake, D., Louie, P. K., Luk, C. W., Simpson, I., and Xu, Z.: Oxidative capacity and radical chemistry in the polluted atmosphere of Hong Kong and Pearl River Delta region: analysis of a severe photochemical smog episode, Atmos. Chem. Phys., 16, 9891-9903, 2016.

25   Yang, X., Xue, L., Wang, T., Wang, X., Gao, J., Lee, S., Blake, D. R., Chai, F., and Wang, W.: Observations and explicit modeling of summertime carbonyl formation in Beijing: identification of key precursor species and their impact on atmospheric oxidation chemistry, J. Geophys. Res.: Atmos., 123, 1426-1440, 2018.

Ye, C., Zhou, X., Pu, D., Stutz, J., Festa, J., Spolaor, M., Tsai, C., Cantrell, C., Mauldin, R. L., and Campos, T.: Rapid cycling of reactive nitrogen in the marine boundary layer, Nature, 532, 489-491, 2016.

30   Ye, C., Zhou, X., Pu, D., Stutz, J., Festa, J., Spolaor, M., Tsai, C., Cantrell, C., Mauldin III, R. L., and Weinheimer, A.: Tropospheric HONO distribution and chemistry in the southeastern US, Atmos. Chem. Phys., 18, 9107-9120, 2018.

Yu, Y., Galle, B., Panday, A., Hodson, E., Prinn, R., and Wang, S.: Observations of high rates of NO$_2$-HONO conversion in the nocturnal atmospheric boundary layer in Kathmandu, Nepal, Atmos. Chem. Phys., 9, 6401-6415, 2009.

Zhang, N., Zhou, X., Shepson, P. B., Gao, H., Alaghmand, M., and Stirm, B.: Aircraft measurement of HONO vertical profiles
35   over a forested region, Geophys. Res. lett., 36,172-173, 2009.

Zhou, X., Civerolo, K., Dai, H., Gu, H., Schwab, J., and Demerjian, K.: Summertime nitrous acid chemistry in the atmospheric boundary layer at a rural site in New York State, J. Geophys. Res.: Atmos., 107, ACH-1-ACH 13-11, 2002.

Zhou, X., Gao, H., He, Y., Huang, G., Bertman, S. B., Civerolo, K., and Schwab, J.: Nitric acid photolysis on surfaces in low-NO$_x$ environments: significant atmospheric implications, Geophys. Res. Lett., 30 (23), 2217, 2003.

40   Zhou, X., Gu, H., Civerolo, K., Roychowdhury, U., and Demerjian, K. L.: Summertime observations of HONO, HCHO, and O$_3$ at the summit of Whiteface Mountain, New York, J. Geophys. Res.: Atmos., 112, D08311, 2007.

Zhou, Y., Wang, T., Gao, X., Xue, L., Wang, X., Wang, Z., Gao, J., Zhang, Q., and Wang, W.: Continuous observations of water-soluble ions in PM$_{2.5}$ at Mount Tai (1534 m asl) in central-eastern China, J. Atmos. Chem., 64, 107-127, 2010.

Ziemba, L. D., Dibb, J. E., Griffin, R. J., Anderson, C. H., Whitlow, S. I., Lefer, B. L., Rappenglück, B., and Flynn, J.:
45   Heterogeneous conversion of nitric acid to nitrous acid on the surface of primary organic aerosol in an urban atmosphere,

Atmos. Environ., 44, 4081-4089, 2010.
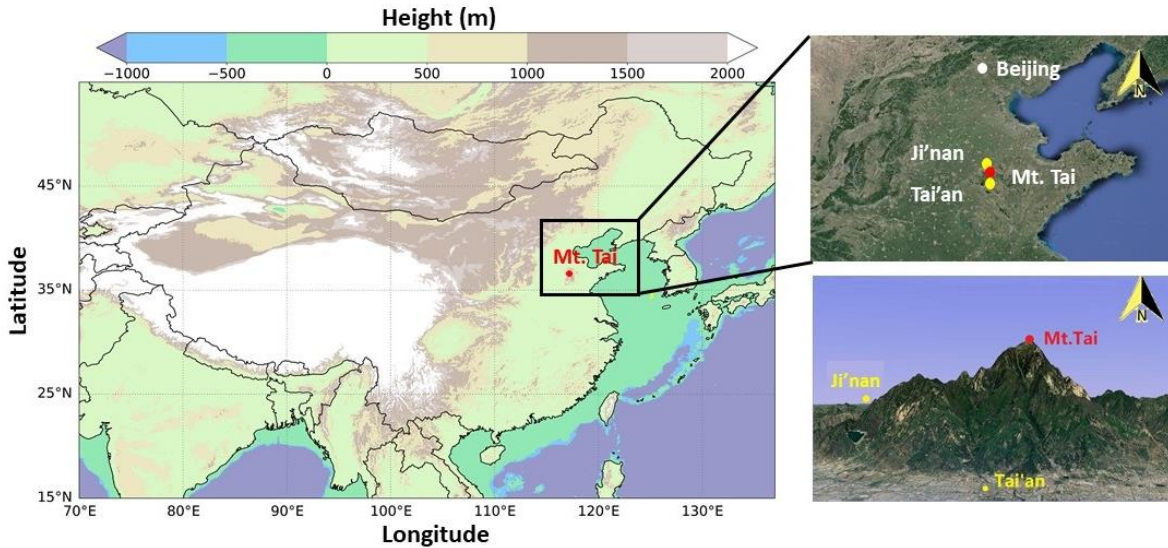
Figure 1. Maps showing the locations of Mt. Tai and the nearby cities. The left map is color-coded by the geographical height from the ETOPO1 Global Relief Model (https://www.ngdc.noaa.gov/mgg/global/). The right-top map represents the North China Plain, and the right-bottom map is the 3-D shape of Mt. Tai with nearby urban regions. The right maps were obtained from Google Earth.
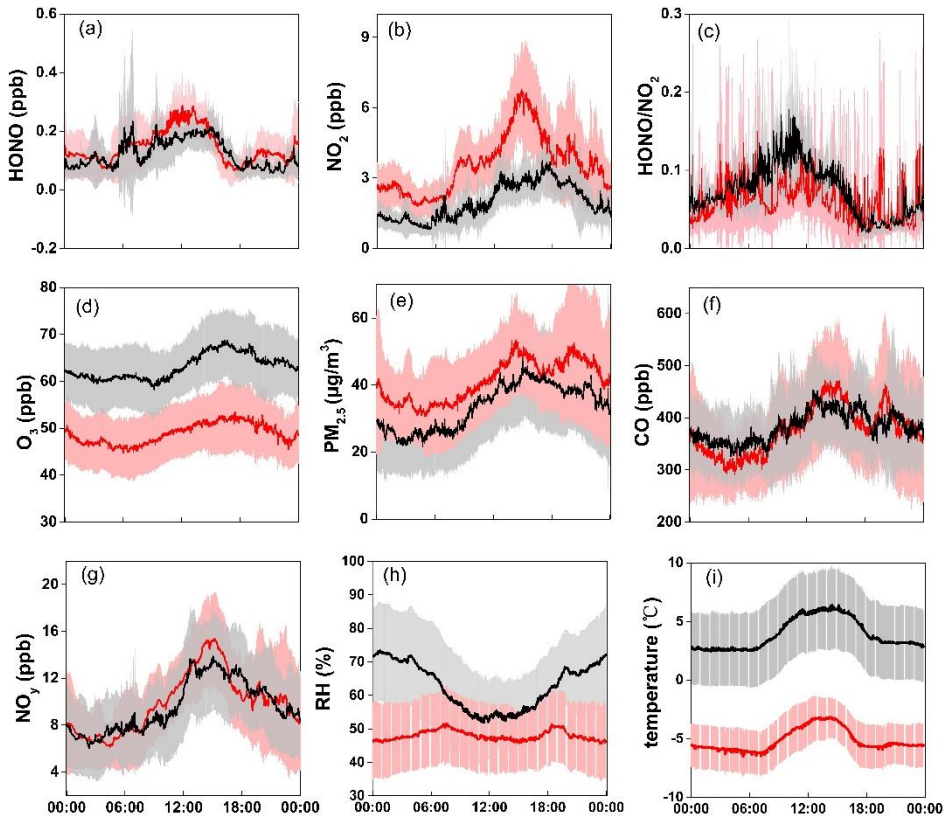
Figure 2. Average diurnal variations of (a) HONO, (b) NO_2, (c) $HONO/NO_2$, (d) O_3, (e) $PM_{2.5}$, (f) CO, (g) NO_y, (h) RH, and (i) temperature in winter (red) and spring (black) at Mt. Tai. Shaded area indicates half standard deviation of the measurement data.
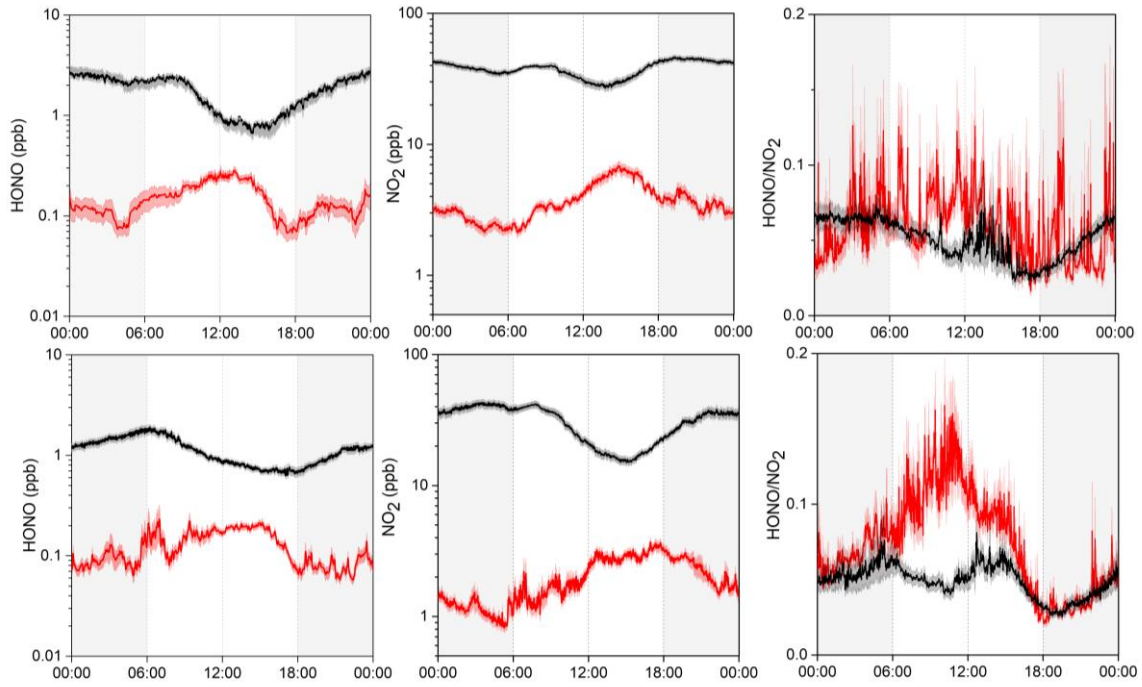
Figure 3. Comparison of the average diurnal variations of HONO, NO₂, HONO/NO₂ at Mt. Tai (red) and in urban Ji'nan (black) in winter (upper panel) and spring (lower panel). Shaded area indicates the standard error of measurement data.
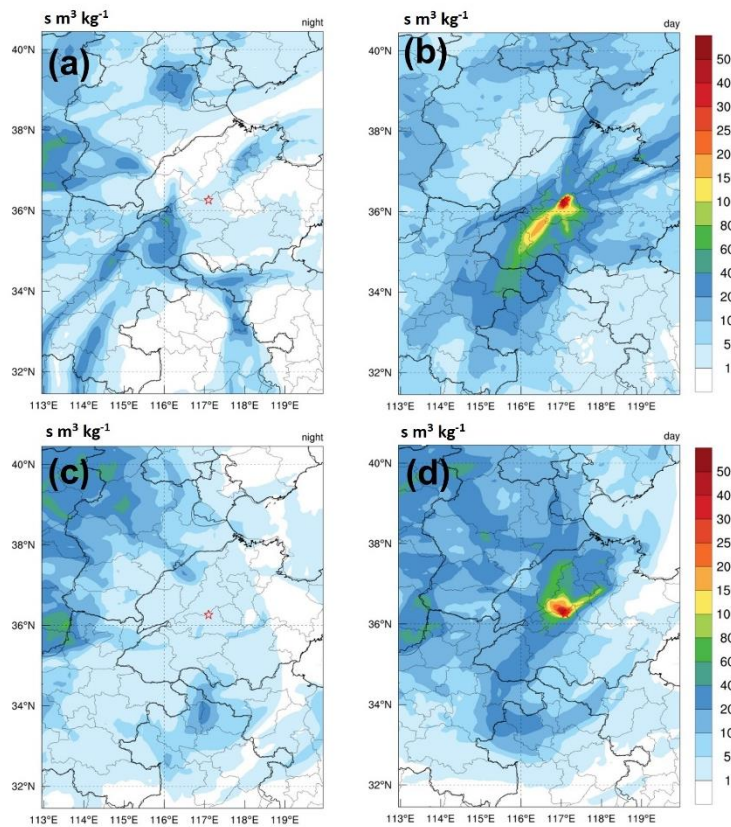
Figure 4. Average distribution of the "footprint" retroplume of the 3-day backward trajectory during (a) spring nighttime (2:00-08:00 LT) and (b) spring afternoon (12:00-18:00 LT); (c) winter nighttime (2:00-8:00 LT) and (d) winter afternoon (12:00-18:00 LT). Note that the horizontal resolution is 0.1°.
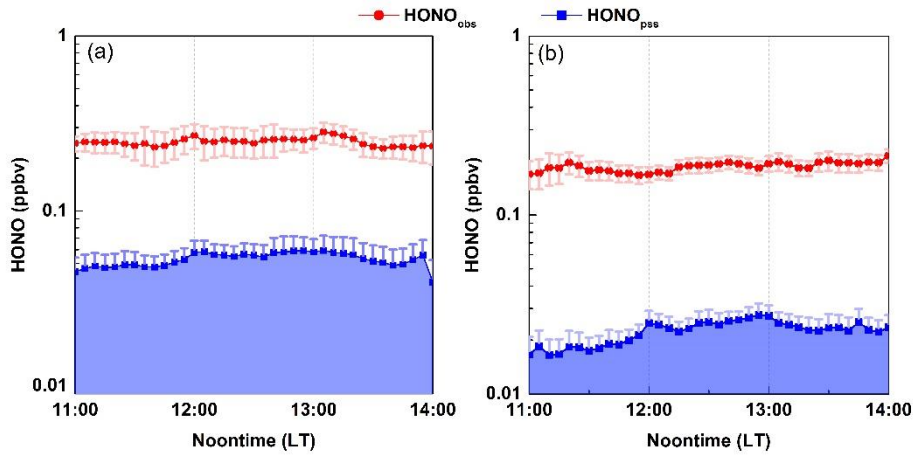
Figure 5. Average noontime [HONO]$_{pss}$ concentrations compared with the observed HONO concentrations in (a) winter and (b) spring. Shaded area indicated the level of [HONO]$_{pss.}$ Error bar indicated the standard error of data.
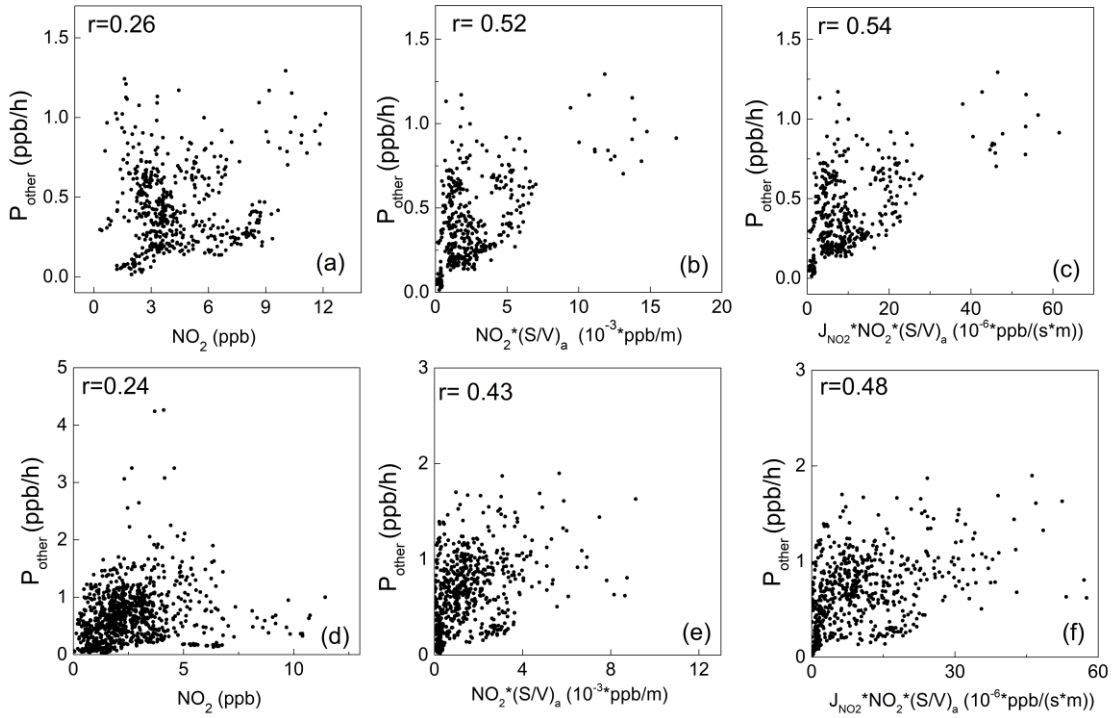
Figure 6. Scatter plots of the additional daytime HONO source strength (P$_{other}$) with NO$_2$, NO$_2$*(S/V)$_a$, and J$_{NO2}$*NO$_2$* (S/V)$_a$ in winter (upper panel) and spring (lower panel).
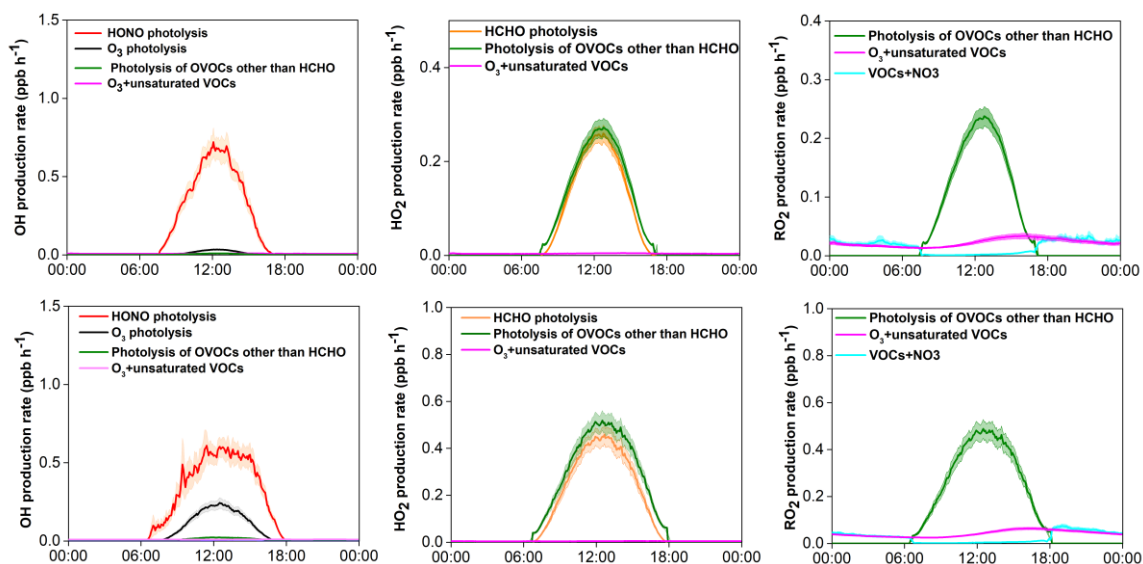
Figure 7. Model-simulated average diurnal variations of major primary sources of OH, HO$_2$ and RO$_2$ at Mt. Tai in winter (upper panel) and spring (lower panel). Shaded area indicates the standard error of the data.
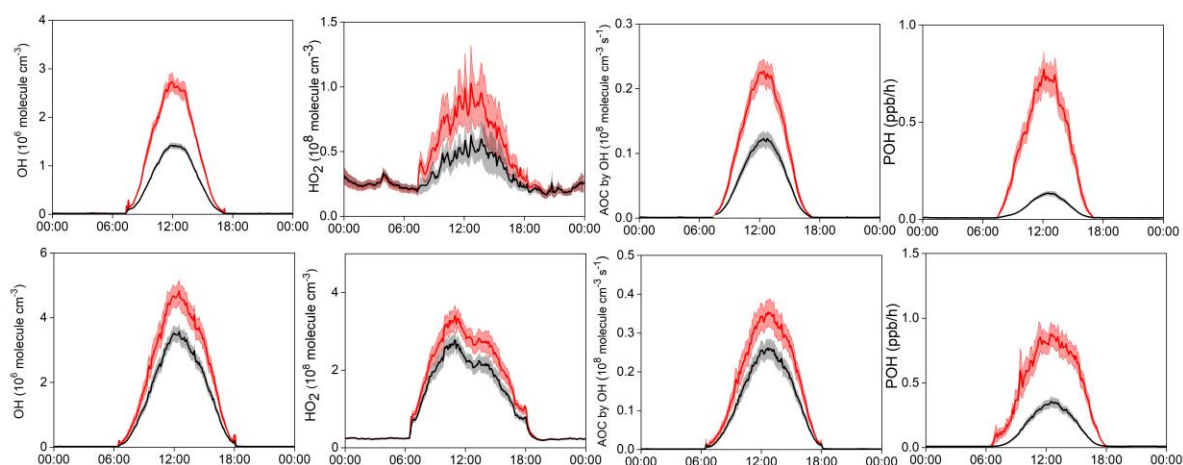
Figure 8. Model-simulated average diurnal variations of OH, HO$_2$, AOC, and primary OH production rate (P$_{OH}$) at Mt. Tai in winter (upper panel) and spring (lower panel), with (red) and without (black) constraints of HONO measurement data. Note that the model only considers the homogenous HONO formation from OH+NO reactions. Shaded area indicates the standard error.

Table 1. Statistics (average ± standard deviation) of trace gases, PM$_{2.5}$, and meteorological parameters measured at Mt. Tai in winter 2017 and spring 2018.

Parameter	2017 winter			2018 spring		
	All data	Daytime	Nighttime	All data	Daytime	Nighttime
HONO (ppb)	0.15±0.15	0.18±0.15	0.11±0.14	0.13±0.15	0.16±0.18	0.09±0.12
NO$_2$ (ppb)	3.59±2.98	4.21±3.06	2.92±2.75	2.00±1.91	2.29±1.99	1.72±1.77
NO (ppb)	0.77±1.19	1.23±1.32	0.05±0.04	0.26±0.35	0.39±0.40	0.09±0.12
NO$_X$ (ppb)	4.64±3.78	5.62±4.05	2.99±2.53	2.18±2.09	2.58±2.26	1.77±1.81
NO$_y$ (ppb)	9.89±7.25	11.30±6.67	8.61±7.22	9.61±7.31	10.61±7.62	8.63±6.84
O$_3$ (ppb)	49±12	49±12	48±12	63±14	64±14	63±14
PM$_{2.5}$ (μg/m^3)	41.1±28.2	41.9±24.3	40.3±31.7	33.7±26.7	35.9±26.3	31.6±27.0
SO$_2$ (ppb)	3.8±4.2	3.8±2.0	3.8±5.6	1.6±1.6	2.1±1.8	1.1±1.2
CO (ppb)	376±193	393±187	358±197	382±161	395±162	170±159
RH (%)	48±20	48±20	48±21	60±26	55±24	66±27
Temperature (°C)	-5.2±3.8	-4.6±3.8	-5.7±3.6	4.3±6.4	5.1±6.5	3.2±6.0
Pressure (hpa)	849.0±0.3	849.1±0.3	849.2±0.3	846.9±0.3	847.1±0.3	846.7±0.3

Daytime period: 06:00-18:00 LT; Nighttime period: 18:00-06:00 LT.

Table 2. Comparison of ambient HONO concentration levels observed at Mt. Tai with previous studies at both surface and high-elevation sites

Type	Site Location	Period	HONO (ppb) Mean±SD	References
	Beijing, China (urban)	Sep -Oct 2015	2.27±1.82	Wang et al., 2017
	Beijing, China (urban)	3 Jan -27 Jan 2016	1.05±0.89	Wang et al., 2017
	Beijing, China (urban)	Apr.-May 2016	1.05±0.95	Wang et al., 2017
	Beijing, China (urban)	Jun-July 2016	1.38±0.90	Wang et al., 2017
	Ji'nan, China (urban)	Sep-Nov 2015	0.78±0.60	Li et al., 2018a
Ground level	Ji'nan, China (urban)	Dec 2015-Feb 2016	1.75±1.62	Li et al., 2018a
observations in China	Ji'nan, China (urban)	Mar-May 2016	1.16±0.90	Li et al., 2018a
	Ji'nan, China (urban)	Jun-Aug 2016	1.12±0.93	Li et al., 2018a
	Wangdu, China (rural)	Jun-Jul 2014	0.91±0.48	Liu et al., 2019
	Guangzhou, China (urban)	Jun 2006	2.80	Qin et al., 2009
	Xinken, China (rural)	13 Oct-2 Nov.2004	1.20	Su et al., 2008b
	Back Garden, China (rural)	Jul 2006	0.76	Li et al., 2012
	Shanghai, China (rural)	Oct 2004-Jan 2005	1.1±1.0	Cui et al., 2018
	Whiteface Mountain, USA (1483 m a.s.l.)	14 Jun-20 Jul 1999	0.046	Zhou et al., 2007
	Summit, Greenland (3200 m a.s.l.)	2 Jul-4 Jul 1999	0.009	Dibb et al., 2002
	Hohenpeissenberg, Germany (980 m a.s.l.)	03 Jul – 12 Jul 2002	0.039	Acker et al., 2006
	Mt.Brocken, Germany (1142 m a.s.l.)	29 Jun –14 Jul 2004	0.063	Acker et al., 2006
		19 Jun –4 Jul 1999	0.056	Acker et al., 2001
High-altitude	North Atlantic Ocean (<2500 m a.s.l.)	5 July 2013	0.011±0.002	Ye et al., 2016
Observations around the world		8 July 2013	0.009±0.002	Ye et al., 2016
	Northern Michigan (1000 m-1900 m.)	30 Jul - 6 Aug 2007	0.009	Zhang et al., 2009
	Northern Italy (300-1000 m a.g.l.)	12 Jul 2012	~0.15	Li et al., 2014
	Southeastern US (>1500 m a.g.l.)	1 Jun -15 Jul 2013	0.006±0.003	Ye et al., 2018
	Mt. Tai, China (1534 m a.s.l)	Nov-Dec 2017	0.15±0.15	This study
		Mar-Apr 2018	0.13±0.15	This study

Table 3. Summary of major primary sources of OH, HO$_2$ and RO$_2$ radicals simulated by MCM model.

Radical primary source [a]		2017 winter		2018 spring	
		Rate [b] (ppb/h)	Proportion (%) [c]	Rate (ppb/h) [b]	Proportion (%) [c]
P$_{OH}$	O$_3$ photolysis	0.022	1.9	0.178	9.0
	HONO photolysis	0.520	44.4	0.511	25.8
	OVOCs photolysis	0.007	0.6	0.018	0.9
	O$_3$ + unsaturated VOCs	0.009	0.7	0.010	0.5
P$_{HO2}$	HCHO photolysis	0.193	16.5	0.374	18.9
	OVOCs photolysis	0.210	17.9	0.434	21.9
	O$_3$ + unsaturated VOCs	0.004	0.4	0.005	0.2
P$_{RO2}$	OVOCs	0.182	15.5	0.407	20.5
	VOCs+NO$_3$	0.002	0.2	0.004	0.2
	O$_3$ + unsaturated VOCs	0.023	2.0	0.042	2.1

[a] OVOCs photolysis denotes the photolysis of OVOCs other than formaldehyde.

[b] Rate is the mid-day (9:00-15:00 LT) average radical production rate.

[c] Proportion is the ratio of the target radical source to the total quantified radical primary production rates.